Cement and Concrete Research 41 (2011) 510–519

Contents lists available at ScienceDirect

Cement and Concrete Research

journal homepage: http://ees.elsevier.com/CEMCON/default.asp

In situ time-resolved X-ray diffraction of tobermorite formation in autoclaved aerated concrete: Influence of silica source reactivity and Al addition

Kunio Matsui [a,*], Jun Kikuma [b], Masamichi Tsunashima [b], Tetsuji Ishikawa [b], Shin-ya Matsuno [b], Akihiro Ogawa [a], Masugu Sato [c]

[a] Construction Materials Laboratory, Asahi-KASEI Construction Materials Corporation, 106 Someya, Sakai, Ibaraki 306-0493, Japan
[b] Analysis and Simulation Center, Asahi-KASEI Corporation, 2-1 Sameshima, Fuji, Shizuoka 416-8501, Japan
[c] Industrial Application Division, SPring-8/JASRI, 1-1-1 Kouto, Sayo, Hyogo 679-5198, Japan

ARTICLE INFO

Article history:
Received 13 October 2010
Accepted 26 January 2011

Keywords:
Calcium silicate hydrate (C-S-H) (B)
X-ray diffraction (B)
Hydrogarnet (D)
Portland Cement (D)
Tobermorite (unlisted)

ABSTRACT

The hydrothermal formation of tobermorite during the processing of autoclaved aerated concrete was investigated by *in situ* X-ray diffraction (XRD) analysis. High-energy X-rays from a synchrotron radiation source in combination with a newly developed autoclave cell and a photon-counting pixel array detector were used.

To investigate the effects of the silica source, reactive quartz from chert and less-reactive quartz from quartz sand were used as starting materials. The effect of Al addition on tobermorite formation was also studied. In all cases, C-S-H, hydroxylellestadite and katoite were clearly observed as intermediates.

Acceleration of tobermorite formation by Al addition was clearly observed. However, Al addition did not affect the dissolution rate of quartz. Two pathways, via C-S-H and katoite, were also observed in the Al-containing system. These results suggest that the structure of initially formed C-S-H is important for the subsequent tobermorite formation reactions.

1. Introduction

Recently, the demand for improved heat insulation of buildings has been increasing; accordingly, autoclaved aerated concrete (AAC) has attracted attention as a construction material because of its excellent heat insulation properties [1,2]. A typical process for the production of AAC includes hydrothermal treatment of a mixture of quartz sand, lime, cement, gypsum and other additives at high temperature (typically, 180–200 °C) under saturated steam pressure, which results in the formation of crystalline calcium silicate hydrates, namely, tobermorite ($Ca_5Si_6O_{16}(OH)_2{\cdot}4H_2O$) [1,3–7]. Both the quantity and crystallinity of tobermorite formed in AAC have been reported to affect the mechanical properties of AAC significantly [4–7]. Therefore, understanding the mechanism of tobermorite formation during hydrothermal treatment (i.e., the autoclave process) is important in AAC production.

The phase evolution of calcium silicate hydrates under hydrothermal conditions, especially the formation of tobermorite, has been extensively studied [8–42]. Several kinetic approaches have also been attempted to clarify the mechanism of tobermorite formation [14,15,35–42]. It is well known that the reactivity of the silica source [8–15], the addition of Al compounds [11,16–29,31,42], the addition of alkali [11,16,28–30] and the addition of sulfate compounds [19,31–34] strongly affect tobermorite formation. As starting material, a highly reactive silica source such as amorphous silica enhances the polymerization of C-S-H, which precedes tobermorite formation, consequently inhibiting the rearrangement of C-S-H to tobermorite [8,9,15,20]. On the other hand, the presence of Al slows the initial formation of C-S-H by reducing the solubility of quartz, which then accelerates tobermorite formation from C-S-H [16,18,20,22,42]. In addition, this inhibits the conversion to xonotlite [9,29], extending the temperature range over which tobermorite exists. These processes are more complex in industrial AAC production, which includes cement as starting material, and the formation mechanism of tobermorite is not thoroughly understood for such processes.

For investigating the formation process, X-ray diffraction (XRD) is a useful technique, but it is difficult to quantify non-crystalline phases, for example, calcium silicate hydrate (C-S-H), which is an important intermediate in the tobermorite formation process. XRD has been used in many *ex situ* studies, in which specimens were taken out from the autoclave at various stages of the reaction. However, such *ex situ* approaches may include ambiguity caused by undesired reactions during the cooling process.

Therefore, an *in situ* approach is more desirable for understanding the reaction in detail. Several *in situ* approaches have been reported for monitoring hydrothermal reactions, cement hydration and pozzolanic reactions by means of transmission XRD [42–48], transmission energy-dispersive XRD [42,49–52], and neutron

---

[*] Corresponding author. Tel.: +81 280 87 5247; fax: +81 280 87 5249.
E-mail address: matsui.kj@om.asahi-kasei.co.jp (K. Matsui).

0008-8846/$ – see front matter © 2011 Elsevier Ltd. All rights reserved.
doi:10.1016/j.cemconres.2011.01.022

diffraction [41]. In these XRD studies, synchrotron radiation has been utilized, taking advantage of its high intensity and high photon energy, which allow the X-rays to penetrate samples of an appropriate thickness. Most of the reaction cells used in these studies were quite small, for example, capillary tubes or thin pipes, because such small cells make pressure sealing easier. However, the accuracy of temperature and pressure control in the cell is insufficient because direct monitoring of these parameters is difficult inside small cells. It is also difficult separate the sample and the water (the source of steam) in the experimental setups using these cells; however, in AAC production it is important that the steam be supplied constantly to the sample throughout the reaction.

We have conducted *in situ* time-resolved XRD analysis of the autoclave process using a newly developed cell in combination with high-energy X-rays from a synchrotron radiation source. In this way, the formation reactions of tobermorite could be successfully observed [53,54]. Our findings suggested that at least two reaction pathways are possible for the formation of tobermorite in the AAC system.

In the present study, we investigated the effects on the reactions of silica source reactivity and Al addition. The mechanisms of tobermorite formation in these systems are discussed.

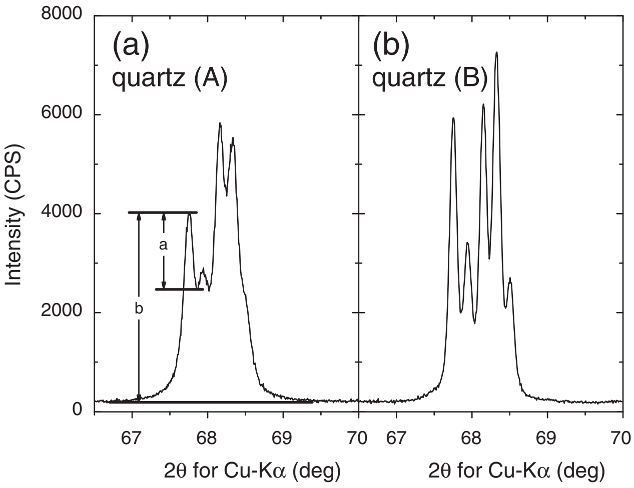

Fig. 1. XRD patterns for quartz (A) and (B), and the calculation method of the crystallinity index (=a/b) on the pattern of quartz (A).

2. Experimental

2.1. Materials and sample preparation

Two types of silica sources, crushed quartz (A) and (B), were used in this study. Quartz (A) originated from chert rock from Fukui, Japan, and consisted of small quartz crystals of several micrometers in grain size. Quartz (B) was natural quartz sand from Vietnam, and consisted of large quartz crystals of several hundred micrometers in grain size. The average particle sizes (d_{50}) of quartz (A) and (B) after crushing were 30.3 μm and 28.3 μm, respectively. The chemical composition and crystallinity index of the two quartz samples are listed in Table 1. Here, the crystallinity index (C.I.) was determined by the method proposed by Hattori and Umeda [55], which is based on Murata and Norman's method [56]. XRD patterns of quartz (A) and (B), and the method of calculating C.I. are shown in Fig. 1. The index is a measure of the alkali–silica reaction (ASR) in concrete [57]. The index decreases with increasing reactivity between quartz and alkali solution. Therefore, the indices in Table 1 signify that the reactivity of quartz (A) is higher than that of quartz (B).

The starting materials were mixtures of 54.4 wt.% silica source (quartz (A) or quartz (B)), 4.7 wt.% quicklime (Kawai Sekkai, Ogaki, Japan), 38.9 wt.% high-early-strength Portland cement (HPC, Ube Mitsubishi, Tokyo, Japan) and 2.0 wt.% gypsum (research grade; Wako, Osaka, Japan). As the Al additive, γ-Al_2O_3 (research grade; Wako) was added to the mixtures. The chemical composition of HPC determined by XRF and the mineral composition calculated using Bogue equation [58] are shown in Tables 2 and 3, respectively. Five mixtures were used in this study, with different silica source and Al content. Table 4 shows silica source and Al content in these mixtures. For all mixtures, the molar ratio of Ca/(Si + Al) was 0.53. Aluminum in the mixtures without added aluminum comes from the aluminate phase in the cement and impurities in the quartz. These mixtures were fully mixed in the presence of water at 50 °C for several minutes using a motor-driven blade stirrer. The water-to-solid ratio was 0.75 by weight. For each run, the mixture slurry was poured into a plastic beaker, sealed in a plastic bag and kept at 60 °C for more than 12 h for the cement in the mixture to become hydrated. The hydrated mixture, so-called pre-cured cake, was then cooled, and cut into specimens with dimensions of 6 mm × 18 mm and thickness of 3.0 mm, immediately before the *in situ* measurement was conducted. In this study, a foaming agent such as Al metal powder, which is commonly used in the production of AAC, was not used to avoid non-uniformity of the X-ray transmission thickness of the samples.

2.2. In situ XRD measurements

In situ XRD measurements at an X-ray energy of 30 keV were carried out at the BL19B2 beamline of SPring-8 (a synchrotron radiation facility in Hyogo, Japan). The X-ray beam size was set to 0.8 mm × 0.12 mm. The autoclave cell is made of stainless steel and consists of a rectangular parallelepiped main body (capacity: 35 cm^3) and a lid. Two beryllium windows (0.5 mm thick, 4 mm and 20 mm in diameter) are firmly welded on the center of each sidewall. The lower part of the cell is used as a water reservoir, typically filled with 5 cm^3 of distilled water. A sample piece is placed on top of the water reservoir using a mounting stand so that the sample does not contact with the water directly. Two thermocouples are inserted into the cell through the lid using compression pipe fittings, in order to monitor both the vapor temperature near the sample and the water temperature. A digital pressure sensor is also connected to the lid in

Table 1
Chemical composition (wt.%) and crystallinity index (C.I.) of quartz sources.

	Quartz (A)	Quartz (B)
SiO_2	96.86	96.77
Al_2O_3	1.18	0.98
Fe_2O_3	0.90	1.05
CaO	0.00	0.01
MgO	0.12	0.05
Na_2O	0.04	0.05
K_2O	0.30	0.44
TiO_2	0.04	0.61
C.I.	0.38	0.67

Table 2
Chemical composition of HPC (wt.%).

SiO_2	CaO	Al_2O_3	SO_3	Fe_2O_3	K_2O	MgO	Na_2O
20.3	65.2	5.2	3.0	2.6	0.4	0.9	0.2

Table 3
Mineral composition and Blaine surface area of HPC.

Mineral composition calculated using Bogue equation (wt.%)				Blaine surface area (cm^2/g)
C_3S	C_3S	C_3A	C_4AF	
63.9	10.1	9.4	7.9	4590

Table 4
Silica source and Al content in samples.

Sample no.	A-0	A-2.5	A-5	B-0	B-5
Silica source	Quartz (A)	Quartz (A)	Quartz (A)	Quartz (B)	Quartz (B)
Al addition (mol%)	0	2.5	5.0	0	5.0
Al/(Al + Si) molar ratio	0.037	0.063	0.088	0.037	0.088

the same way. A diaphragm pump and a needle valve are connected to the branched line of the pressure sensor for the removal of the air inside. Further details of the cell are described in our previous reports [53,54].

The autoclave cell containing the sample and water was set in a copper heater block. First, the temperature was raised to 100 °C at a ramping rate of 2 °C/min. The temperature was held at 100 °C for 15 min. During this period, the cell was evacuated for a few seconds, and about 95% of the air was removed from the cell. After the steam pressure built up again at 100 °C, the first XRD measurement was conducted. After 15 min at 100 °C, the temperature was raised to 190 °C at a ramping rate of 1 °C/min, and then held at 190 °C for 12 h. The pressure inside the cell was confirmed to be saturated steam pressure in all experiments.

During this process, the XRD measurements were conducted using a photon-counting pixel array detector, PILATUS 100 K (DECTRIS). The detector was placed downstream at a sample-to-detector distance of 777 mm. Because the detector area (width: 34 mm; height: 84 mm) was not large enough to measure the entire diffraction angle range of interest, three images were acquired for each measurement by moving the detector along the vertical direction such that some part of each adjacent image overlapped. The three images were then connected seamlessly to obtain a long rectangular image. The exposure time was 60 s for each image, and the measurement interval was 4.15 min, including the time for repositioning the detector. During the exposure time, the cell, together with the heater block, was oscillated in the vertical direction at an amplitude of 3.0 mm and a rate of 0.6 mm/s to average the measurements over a larger area of the sample. For each sample, 196 measurement cycles were conducted during the autoclaving time of 13.5 h. The arc-shaped diffraction patterns were obtained for a $1/d$ range of 0.5–6.5 nm^{-1} [54].

2.3. Data analysis

Typically, the sector average of the arc-shaped two-dimensional pattern is calculated to obtain one-dimensional diffraction patterns. However, for quartz and portlandite, the arc-shaped diffraction patterns mainly consist of a number of diffraction spots from crystalline particles originating from the starting materials. This means that the diffraction intensity of these two constituents varies largely depending on the number and size of the crystalline particles that contribute to the diffraction. In addition, some extremely strong diffraction spots from large crystallite of quartz and portlandite were observed. We eliminated the pixel data for such spots before calculating the sector average to prevent a few strong spots from dominating the averaged peak intensities. This procedure was done in only a few cases, in which the fluctuation of the intensity curve was relatively large. It was confirmed that overall intensity profiles before and after this procedure were not considerably changed.

Hence, the absolute value of the normalized intensity for quartz and portlandite cannot be compared directly between different samples in this experiment. Therefore, for quartz and portlandite, changes in only relative intensity are considered. This is not the case for other constituents that are formed during the autoclave process. However, it should be noted that anhydrite tends to exhibit non-uniform diffraction rings in image data, although this does not largely affect the time-dependent intensity data.

Two-dimensional image data were sector-averaged to produce one-dimensional diffraction patterns. Peak intensities were calculated from peak areas after being normalized by the transmitted beam intensity. Peak positions were defined as the middle point of two half-maximum positions, which were calculated from the interpolation of the nearest two data points.

Non-crystalline C-S-H is also formed by hydration of cement and is well known as a major precursor to tobermorite formation [8–20,31–34,38–42,59]. To clarify the mechanism of tobermorite formation, it is important to observe the C-S-H phase closely. Generally, it is difficult to investigate the amount of non-crystalline materials by using *ex situ* XRD during the reaction process because the intensity of the amorphous halo can be affected by the background intensity, which can vary depending on the part of the sample analyzed or on the sample preparation method. In an *in situ* experiment, however, the same portion of the sample is continuously measured throughout the experiment. This allows slight changes in amorphous intensity to be detected. The integrated intensity from 3.427 to 3.434 nm^{-1} (no background subtracted) was regarded as the C-S-H intensity in our previous reports [53,54]. In the present study, this method was used to estimate relative changes in the quantity of C-S-H with hydration time in the same experiment.

3. Results and discussion

3.1. Phase evolution

The time-resolved XRD data set for sample A-0 is shown in Fig. 2. Several constituents involved in the reaction were clearly observed. The time dependence of the relative peak intensities of major constituents for samples A-0, A-2.5 and A-5 is plotted in Fig. 3(a), (b) and (c), respectively. The intensities for samples B-0 and B-5 are plotted in Fig. 4(a) and (b), respectively. The sum of the (211) and (002) peak intensities for HE, and the sum of the (211) and (220) peak intensities for KA are plotted to obtain larger peak integrals and better statistics. For tobermorite, the (002) and (220) peaks are separately plotted. All data were normalized on the basis of XRD measurements of the same sample in our laboratory after *in situ* XRD. Detail of the method is as follows: first, the tobermorite intensity in the final products of each sample after *in situ* measurement was measured by laboratory XRD with exactly same experimental condition, by which the intensity of different samples can be compared directly. Second, those intensities were compared with the data of the last cycle of *in situ* experiments and coefficients to correlate two XRD patterns were determined for each sample. And then, all data were normalized using the coefficients.

It should be noted that the mass absorption coefficients for samples in this study are nearly identical because the differences in chemical compositions between samples are due to only a few % of Al_2O_3 which replaces SiO_2. Thus, we consider that it is possible to compare the normalized intensities between different samples.

In all experiments, monosulfate (MS: $Ca_4Al_2O_6(SO_4)$–$14H_2O$, PDF Card 42-0062) and portlandite ($Ca(OH)_2$) were observed at the beginning of the autoclave process, and decreased as the reactions proceeded; MS and portlandite then completely disappeared. Quartz initially decreased slowly, and the rate of decrease became slightly faster in the middle and then became slower again toward the end. As intermediate phases katoite (KA: $Ca_3Al_2(SiO_4)_{3-x}(OH)_{4x}$; $x = 1.5$ to 3.0, PDF Cards No. are listed in Section 3.3), a kind of hydrogarnet, was observed in the heating process, subsequently, hydroxylellestadite (HE: $Ca_{10}(SiO_4)_3(SO_4)_3(OH)_2$, PDF Card 25-0173) was observed. HE disappeared in all experiments as the reactions progressed; on the other hand, KA decreased slowly and partly remained in some experiments. Tobermorite was first observed when the temperature

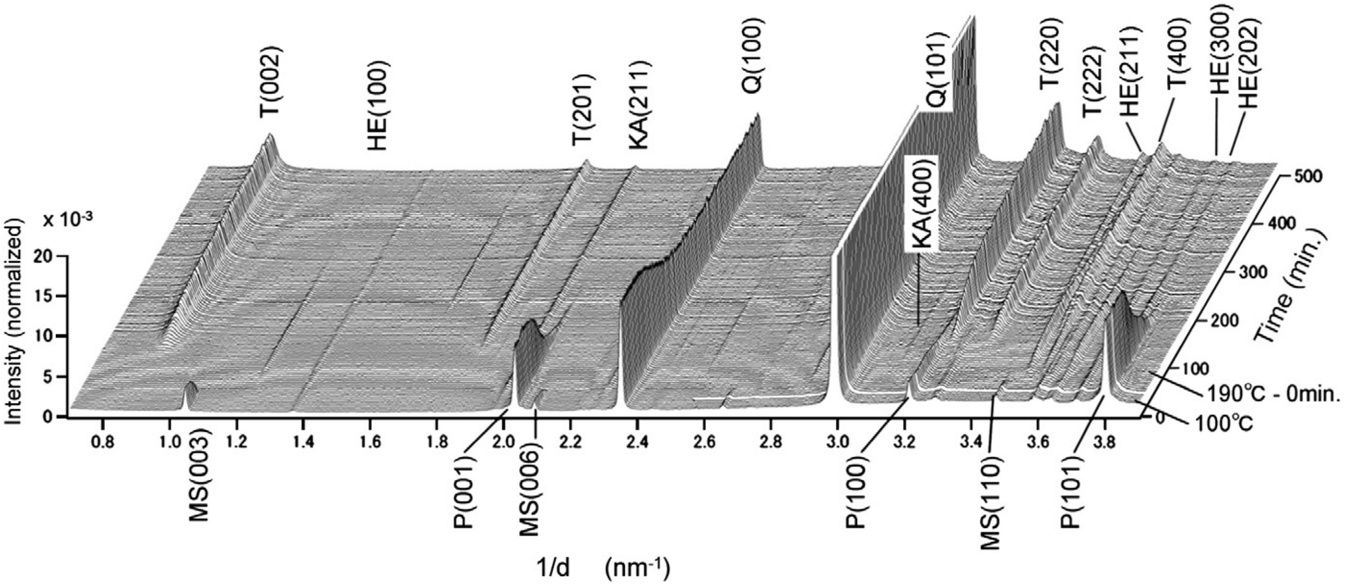

Fig. 2. Stack of time-resolved XRD patterns for A-0. Temperature was increased from 100 to 190 °C and then held at 190 °C for 500 min. T: tobermorite; P: portlandite; Q: quartz; MS: monosulfate; KA: katoite; HE: hydroxylellestadite.

reached 190 °C at the same time as the intensity of C-S-H started to decrease, and the amount of tobermorite increased toward the end of the autoclave process. Anhydrite ($CaSO_4$, PDF Card 06-0226) was first observed at the same time as HE started to decrease and increased gradually until the end. This suggests SO_4^{2-} ions released from HE were involved in the formation of anhydrite. Several studies have reported that HE decomposes into anhydrite and tobermorite under hydrothermal conditions [32,33]. Our results are consistent with these studies.

In the experiments with no Al addition, A-0 (Fig. 3(a)) and B-0 (Fig. 4(a)), the slope of the intensity curve of the (002) reflection of tobermorite for A-0 was larger than that for B-0 in the early stage. The rate for A-0 then decreased sharply from about 200 min and the intensity curve became constant. However, the rate of increase of the tobermorite (002) reflection for B-0 was lower in the early stage, and the formation continued in the late stage. Consequently, both tobermorite (002) and (220) peaks of B-0 were stronger than those of A-0 at the end of the experiment.

For the experiments with Al addition, namely, A-2.5, A-5 and B-5, it was clearly observed that Al accelerated the crystallization of tobermorite and caused tobermorite formation to begin earlier. For the A series, Al accelerated the crystallization of tobermorite in the direction of the *c*-axis selectively. The intensity of the tobermorite (002) for A-2.5 was located between that for A-0 and A-5, indicating that the effect of Al addition increased with the amount of added Al. On the other hand, for the B series, the effect of Al addition was not as strong but the decrease of the formation rate in the late stage was small. As a result, the reaction continued and the final intensity of the tobermorite (002) peak for B-5 was slightly larger than that for B-0. It should be noted that for all experiments with the Al addition, the KA intensities increased in the early stage; thus, Al appeared to contribute strongly to the formation of KA. This effect will be discussed later.

3.2. Tobermorite formation from C-S-H phase

In order to understand the mechanism of tobermorite formation from its relationship with C-S-H, the intensities of C-S-H and tobermorite (002) are plotted in Figs. 5 and 6 for the A and B series, respectively. Because the time of maximum C-S-H intensity corresponded to the starting point of tobermorite formation, and because the tobermorite intensity increased with decreasing C-S-H intensity, it is reasonable to consider that most of the tobermorite phase was formed from the C-S-H phase as described in previous studies [8–20,31–34,38–42,59]. Recently, Houston et al. reported that tobermorite formation proceeded via three steps: formation of amorphous and non-crystalline C-S-H, growth of semi-crystalline tobermorite, and recrystallization of the tobermorite solid [38]. The C-S-H intensity in the case of A-0 remained high even after tobermorite formation, while the final C-S-H intensity in the case of B-0 was nearly equal to the initial intensity. This means that the C-S-H phase remained in the late stage in A-0, and that most of C-S-H formed at the beginning of the autoclave process disappeared and transformed to the tobermorite phase in B-0. As for the effect of Al addition, the acceleration of tobermorite formation was small in the B series, but remarkable in the A series. This has been already observed in Figs. 3 and 4 but is shown more clearly in these figures. Considering the difference in C-S-H intensities at the start and the end of the autoclave process in the case of the A series, we can conclude that Al addition strongly affects the decrease of the C-S-H phase and causes tobermorite formation to begin earlier.

Cement was used as starting materials; the cement phases (C_3S and C_2S) are considered to be hydrated at the beginning of the autoclave process, because the peaks of both phases were not clearly observed and Ca ions are thought to be saturated in the liquid phase. Therefore, it is reasonable to consider that the dissolution of quartz is a rate-limiting process in the early stage of the reaction [14,36,40,41]. To understand the dissolution behavior of quartz, normalized intensities of the quartz (100) reflection in the A and B series are plotted in Fig. 7. As noted in the experimental section, because the absolute values of the intensities for quartz were affected by the coarseness of grains, the data were treated by mask processing. Thus, in these figures the intensities were normalized again so that these intensities at the start point of 190 °C ($t = 90$ min) were same. Here, the rate of the decrease of quartz (A) is greater than that of quartz (B) in the early stage. Because this trend corresponds to the increase of the C-S-H phase (shown in Figs. 5 and 6), Si ions in the liquid phase from the dissolution of quartz take part in the C-S-H formation.

As for the effect of Al addition, it was observed that Al suppressed the dissolution of quartz slightly in the period from 100 to 200 min. As mentioned above, Al slows the initial formation of C-S-H from quartz and CaO because it reduces the solubility of quartz. Several studies have shown that the decreased solubility of quartz results from

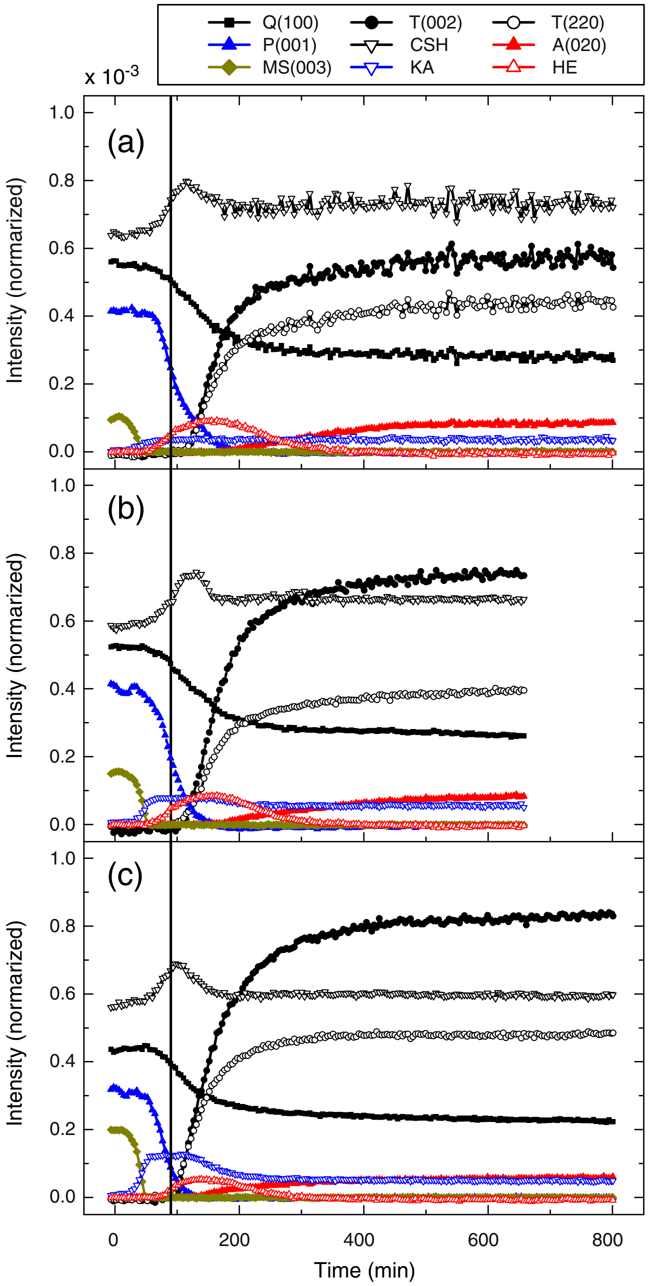

Fig. 3. Time dependence of peak intensities for major constituents during the autoclave process: (a) sample A-0, (b) sample A-2.5 and (c) sample A-5. Intensities of C-S-H are baseline intensities at 3.43 nm^{-1}. T: tobermorite; P: portlandite; Q: quartz; MS: monosulfate; KA: katoite; HE: hydroxylellestadite; A: anhydrite; C-S-H: non-crystalline calcium silicate hydrate. Vertical line at 90 min indicates the time at which the temperature reached constant value (190 °C).

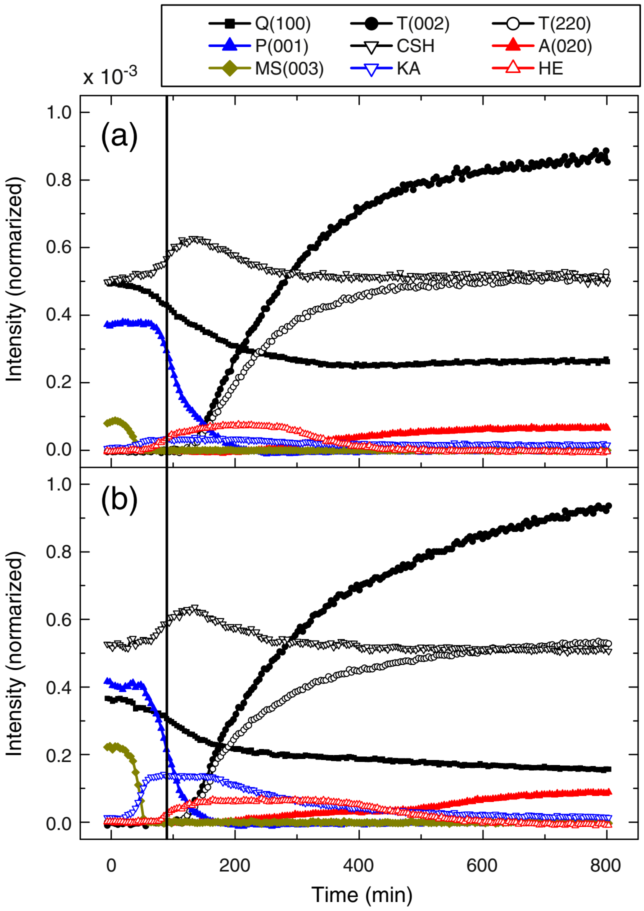

Fig. 4. Time dependence of peak intensities for major constituents during the autoclave process: (a) sample B-0 and (b) sample B-5. T: tobermorite; P: portlandite; Q: quartz; MS: monosulfate; KA: katoite; HE: hydroxylellestadite; A: anhydrite; C-S-H: non-crystalline calcium silicate hydrate. Vertical line at 90 min indicates the time at which the temperature reached constant value (190 °C).

adsorption of Al on the quartz surface [60,61]. However, in the present study the reduced solubility was not observed. One reason for this is that alkali ions in the liquid phase from the cement influenced the dissolution of quartz. In addition, it should be noted that the dissolution of quartz continued after 400 min for only the B-5 sample. This relates to the fact that the rate of tobermorite formation did not decrease in the late stage (Fig. 6). These results suggest that there may be another route to tobermorite formation after the disappearance of C-S-H phase, which will be discussed in following section.

Another reason for the difference in tobermorite formation curves between A series and B series may be the difference in Ca/Si ratio C-S-H gel formed in the early stage of the reaction. Considering high reactivity of quartz A, it would be reasonable to regard that the Ca/Si ratio of C-S-H is lower in A series (higher Si content). It has been reported that the C-S-H with high Ca/Si ratio tends to have short silicate chains [59,62–66] and is more likely to be transformed into tobermorite than that with low Ca/Si [8,20]. The C-S-H curves in Figs. 5 and 6 indicate that, for A series, there is some C-S-H remaining

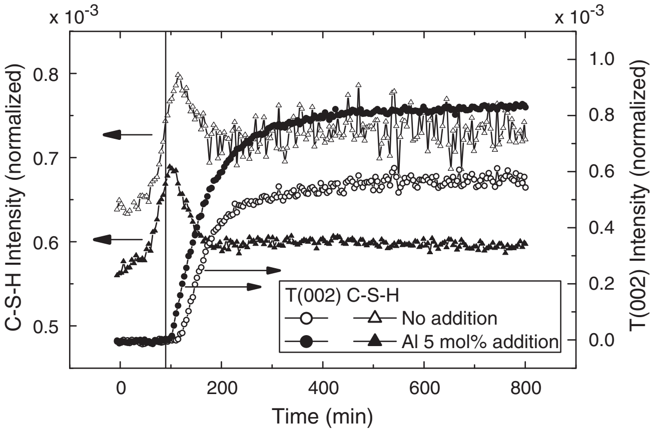

Fig. 5. Time dependence of peak intensities for tobermorite (002) and C-S-H of A series during the autoclave process for A-0 (no Al addition) and A-5 (5 mol% Al addition). Intensities of C-S-H are baseline intensities at 3.43 nm^{-1}. Vertical line at 90 min indicates the time at which the temperature reached constant value (190 °C).

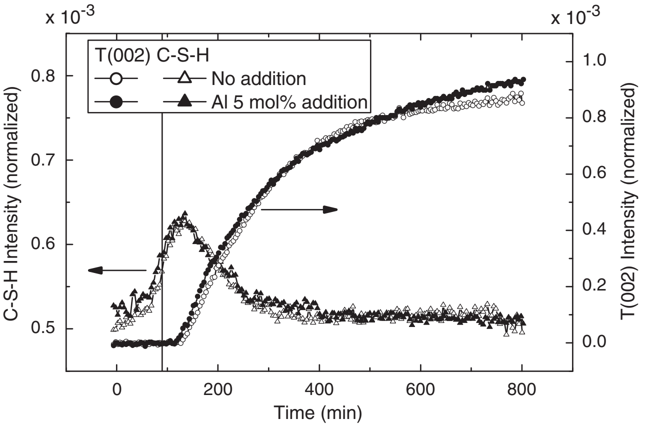

Fig. 6. Time dependence of peak intensities for tobermorite (002) and C-S-H of B series during the autoclave process: B-0 (no Al addition) and B-5 (5 mol% Al addition). Intensities of C-S-H are baseline intensities at 3.43 nm^{-1}. Vertical line at 90 min indicates the time at which the temperature reached constant value (190 °C).

at the end of the reaction, while little C-S-H remaining for B series. This implies the C-S-H in B series have higher Ca/Si ratio, and thus, shorter chain lengths than those in A series.

3.3. Tobermorite formation from KA phase

KA is a type of hydrogarnet, and its chemical composition varies in accordance with Si content in the solid solution. The lattice constant varies continuously with the Si content [67]. Several studies have reported that, for example, when kaolin and lime are used as starting materials [18,68–70], KA is an important intermediate in tobermorite formation. Figs. 8(a) and 9(a) show the time dependence of the tobermorite (002) peak intensity and the sum of KA (211) and (220) peak intensities for the A-0 and A-5 samples, and for the B-0 and B-5 samples, respectively. The KA intensities increased considerably in the early stage, especially for A-5 and B-5. Subsequently, the KA intensities decreased with increasing tobermorite intensity. KA remained until the end in the A series, but almost disappeared in the B series. The rate of decrease of KA for A-5 was higher than that for B-5. This trend corresponds to a higher rate of tobermorite formation in the case of A-5. Thus, in addition to C-S-H, KA is considered to be a precursor to tobermorite formation.

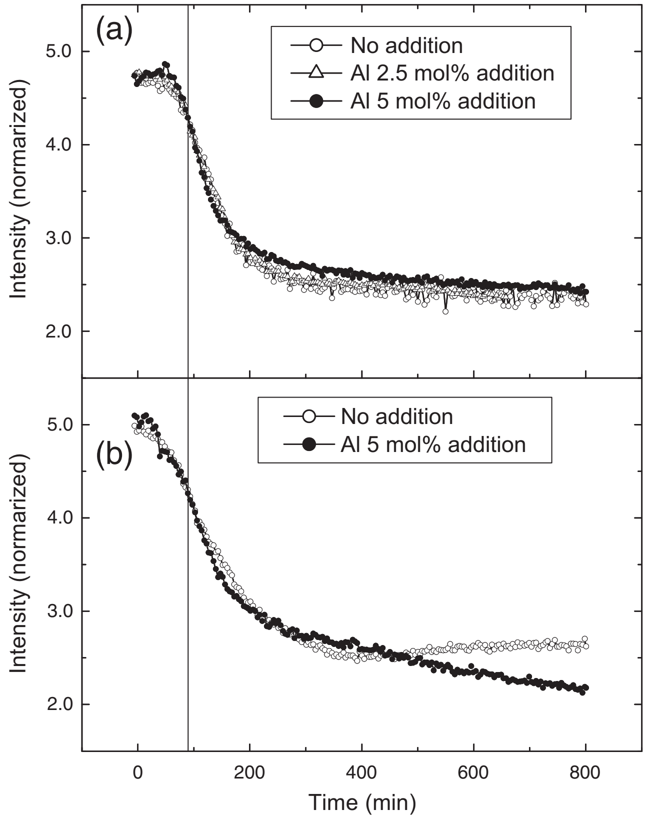

Fig. 7. Time dependence of peak intensities for quartz (100). (a) A series: A-0 (no addition), A-2.5 (2.5 mol% Al addition) and A-5 (5 mol% Al addition). (b) B series: B-0 (no Al addition) and B-5 (5 mol% Al addition). Vertical line at 90 min indicates the time at which the temperature reached constant value (190 °C).

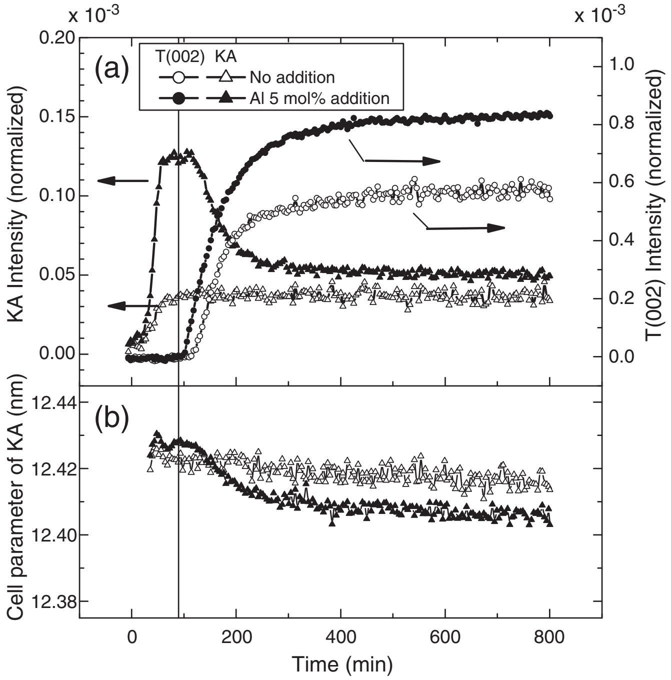

Fig. 8. Time dependence of peak intensities for tobermorite (002) and katoite (211) + (220) of A series during the autoclave process: A-0 (no addition) and A-5 (5 mol% Al addition). Bottom part shows the lattice parameter of katoite. Vertical line at 90 min indicates the time at which the temperature reached constant value (190 °C).

Figs. 8(b) and 9(b) show the time dependence of the lattice parameter of KA for the A-0 and A-5 samples, and for the B-0 and B-5 samples, respectively. The crystal structure of KA is cubic, and the lattice parameter decreases with increasing substitution of SiO_4 for $(OH)_4$ in the hydrogarnet structure. The parameter was calculated from the peak positions of the (211) and (220) reflections. It should be noted that the lattice parameter decreases with decreasing KA intensity. In particular, the parameter for B-5 decreases markedly with reaction time. According to Bennet et al., the substitution of SiO_4 for $(OH)_4$ in KA structure has a linear relationship with the Si concentration in the liquid phase at 25 °C, where KA is at equilibrium [71]. However, the temperature is higher in the present system. If this equilibrium is reached rapidly, it is considered that the concentration of Si ions in the liquid phase will increase with progress of KA decomposition and tobermorite formation.

The time dependence of the KA (211) diffraction peak profile for the B-5 sample is shown in Fig. 10. As the reaction proceeds, the profiles shifted to higher angle. Simultaneously, the intensity decreases while the profile remains symmetrical. This does not mean that only structural parts of KA with higher Si content (lower lattice parameter parts) decompose selectively. It is quite likely that KA decreases with increasing Si substitution into its own lattice. Therefore, it is considered that the concentration of Si ions in the liquid phase increased until the late stage, especially for B-5. On the

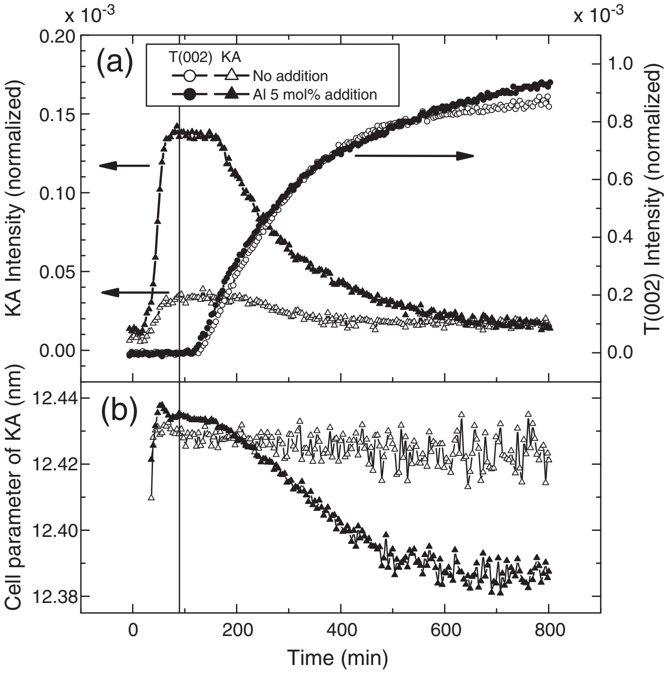

Fig. 9. Time dependence of peak intensities for tobermorite (002) and katoite (211) + (220) of B series during the autoclave process: B-0 (no Al addition) and B-5 (5 mol% Al addition). Bottom part shows the lattice parameter of katoite. Vertical line at 90 min indicates the time at which the temperature reached constant value (190 °C).

other hand, the decrease of the lattice parameter for A-5 is relatively small. This suggests that the remaining C-S-H phase in the A-5 sample dominates the liquid phase composition.

Siauciunas and Baltusnikas have investigated the Si content of hydrogarnet formed in hydrothermal treatment of a mixture of SiO_2, Al_2O_3 and CaO [72]. They found that Si content in hydrogarnet varies according to the type of silica in the starting materials. When quartz was used as a silica source, Si-free hydrogarnet was formed, reflecting the low solubility of quartz. When amorphous silica was used, Si in hydrogarnet corresponded to an x value of 2.5 in $Ca_3Al_2(SiO_4)_{3-x}(OH)_{4x}$. However, in the present work, calculating x from the linear relationship with the lattice parameter at the end of the experiments at 190 °C and from the composition for KA in PDF cards (24-0217, 38-0368, 45-1447, 42-0570, 39-0368), we find x to be 2.22 and 2.08 for B-0 and B-5, and 2.19, 2.17 and 2.09 for A-0, A-2.5 and A-5, respectively. The thermal expansion coefficient of KA in the literature [73] was used to calculate the lattice parameters at 25 °C. All x values found in the present study were lower than the x value for the amorphous silica system in the study of Siauciunas and Baltusnikas; thus, the substitution of Si for $(OH)_4$ in the KA structure is more dominant. Huber et al. have also reported that Si-free hydrogarnet and hydrogrossular/grossular solid solution (katoite) are formed in the tobermorite formation process with Al addition [39]. In addition, they noted that the solid solution phase transformed to the Si-free hydrogarnet as the reaction progressed. In the present work, the higher Si-substitution in KA, regardless of the use of quartz as the silica source, may reflect a higher Si ion concentration in the liquid phase. It is likely that alkali from the cement used as starting material has an effect on the Si ion concentration in the liquid phase.

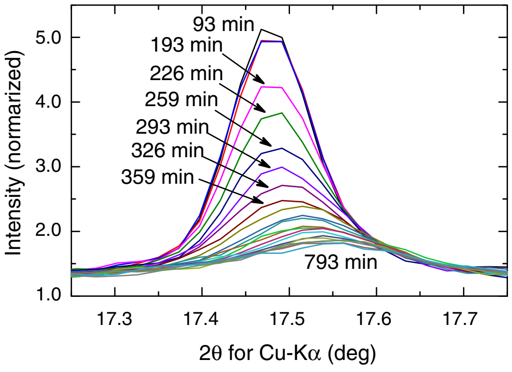

Fig. 10. Change of katoite (211) peak profile for sample B-5 during autoclave process. Numbers on the figure correspond to the time from the start of the reaction.

Klimesh et al. [68,69] reported that KA is the main intermediate phase in the hydrothermal reaction in the metakaolin–quartz–lime system and that the decomposition of KA was accelerated as the size of the quartz particles was decreased. In contrast to the results of Klimesh et al., KA remained until the end of the autoclave process in the system containing a more reactive Si source (A series: Fig. 8(a)). It may be considered that the reaction between KA and quartz (or Si ions in the liquid phase) was slowed by C-S-H, which was formed initially and partly remained in the A series. This reaction inhibition by C-S-H will be discussed in the next section.

Fig. 11(a) and (b) shows the time dependence of the Bragg spacings of tobermorite (002) for A-0, A-2.5 and A-5, and for B-0 and B-5, respectively. The Bragg spacing of tobermorite (002) can be clearly seen to decrease with tobermorite formation, the Bragg spacings of tobermorite (220) were unchanged in all experiments (data not shown). These trends were observed in our previous study as well [54]. Mitsuda et al. [5] investigated the chemical composition of tobermorite crystals in AAC for various autoclaving times. They found that the Ca/(Al + Si) ratio is greater than the stoichiometric value at the early stage of the autoclave process, decreases with the

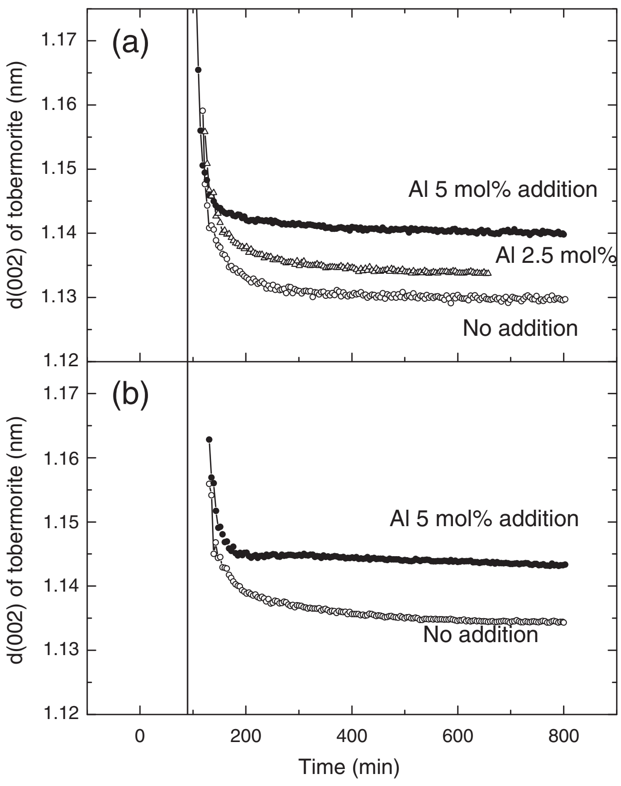

Fig. 11. Time dependence of Bragg spacings of tobermorite (002). (a) A series: A-0 (no addition), A-2.5 (2.5 mol% Al addition) and A-5 (5 mol% Al addition). (b) B series: B-0 (no Al addition) and B-5 (5 mol% Al addition). Vertical line at 90 min indicates the time at which the temperature reached constant value (190 °C).

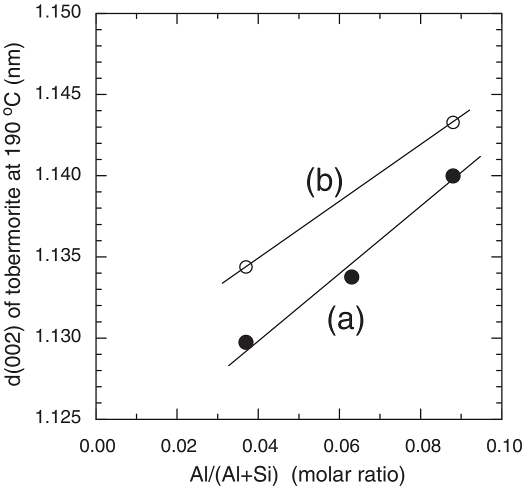

Fig. 12. Relation between Bragg spacings of tobermorite (002) at the end of experiment and Al/(Al + Si) molar ratios calculated from the chemical composition of raw materials for (a) A series and (b) B series.

increasing autoclave time, and then become stable at the stoichiometric value. Assuming that the excess Ca beyond the stoichiometric value can be attributed to the Ca ions in the interlayer region of tobermorite, it is reasonable that the (002) spacing decreased with the reaction time (Fig. 11).

The (002) spacing of tobermorite at the end of the autoclave are shown in Fig. 12. The (002) spacing increased linearly with the addition of Al. It is well known that Al is substituted into the Si-tetrahedra of tobermorite [17,23–29,38,39], as well as that the basal spacing increases with Al content [17,29,39,54]. Fig. 11(a) and (b) shows that the (002) spacing of the samples without Al addition (A-0 and B-0) decreased drastically, then gradually leveled off, decreasing with time until 400 min, whereas the (002) spacing of the samples with Al addition (A-5 and B-5) leveled off earlier. Consequently, the differences between the spacing with and without Al became larger from about 150 min. Therefore, it is reasonable to consider that Al was gradually substituted into the tobermorite lattice from about 150 min. This corresponds to the decrease of KA shown in Figs. 8(a) and 9(a), implying the KA phase is the source of Al that is substituted into the tobermorite lattice. In addition, the difference of the lattice parameters shown by the two lines in Fig. 12 is considered to correspond to the difference between amounts of remaining KA of in A and B series at the end of experiments.

3.4. Formation mechanism of tobermorite

Our previous study has suggested that tobermorite crystallized through two pathways under hydrothermal reaction conditions [53,54]. Considering previous studies together with the present results, we can summarize the two pathways as follows:

$$\mathrm{C-S-H} \rightarrow \text{tobermorite} \qquad \text{(I)}$$

$$\mathrm{Quartz, KA, HE, (C-S-H)} \rightarrow \mathrm{Si^{4+}, Ca^{2+}, Al^{3+}, OH^{-}} \rightarrow \text{tobermorite} \qquad \text{(II)}$$

Reaction (I) is a transformation between solid phases, described in the earlier section. On the other hand, reaction (II) is a solid–liquid reaction in which tobermorite crystallizes from the liquid phase. Tobermorite formation via the KA phase, described in the previous section, is part of reaction (II). These two reactions proceed not independently, but rather interdependently. For example, in the case of the A series with reactive silica source, early formation of C-S-H, which is difficult to crystallize to form tobermorite via reaction (I), may slow the dissolution of quartz and/or the decomposition of KA via reaction (II). This role of C-S-H was observed in all experiments using the A series; consequently, reaction (II) did not proceed adequately. Thus, the C-S-H formed in the early stage affected the dissolution of quartz and KA in the late stage. One possible reason for this is that the pH of the liquid phase was lowered by adsorption of alkali on the C-S-H or C-S-A-H surface [74,75]. Another reason would be that C-S-H formed around quartz particles and acted as a physical barrier to quartz dissolution [40].

On the other hand, in the experiment on the B series with a less-reactive silica source, the reactive C-S-H, likely having short chain length as suggested by Sato and Grutzeck [8], is completely crystallized to form tobermorite through reaction (I). After that, because the reaction (II) became predominated in the late stage, the dissolution of quartz and the decomposition of KA continued until the end. From this model, we can conclude that the structure of the initially formed C-S-H controls the two pathways of tobermorite formation.

3.5. Acceleration mechanism on tobermorite formation by Al

According to the above model, acceleration of reaction (I) in the A series by Al (Fig. 5) can be explained as follows. C-S-H that formed before tobermorite became destabilized by Al; this means that the barrier to tobermorite crystallization was diminished by Al. For the B series, on the other hand, the dissolution of quartz was accelerated in the late stage by Al, decreasing the lattice parameter of KA (Fig. 8(b) and 9(b)). This suggests that reaction (I) was completed in the early stage and that the main formation process was shifted to reaction (II) by Al.

It is also important to consider the mechanism of Al-accelerated tobermorite formation on a nanoscale. In the C-S-H structure, Al atoms have coordination numbers of 4, 5 and 6 [76,77]; however, Al has only a coordination number of 4 in the tobermorite structure. In both cases, the Al atoms having coordination number of 4 are substituted preferentially into bridging tetrahedral sites (Q3) at middle chain sites [17,24,26,38,78–80]. In these structures, Al in the tobermorite has a significant effect on the mean length of the silicate chains [30], and negatively influences the degree of silica polymerization [27]. Additionally, Sasaki et al. reported that Al-substituted tobermorite was degraded more easily than Al-free tobermorite during vibratory milling, and they noted that the Al-O binding energy was lower than that of Si-O in the structure [80]. According to these reports, it can be deduced that the formation energy (ΔG) of tobermorite is lowered by the Al substitution for Si.

In the hydrothermal reaction process, Mitsuda et al. [20] have reported that Al significantly accelerates tobermorite crystallization from a silicic acid-lime mixture at 180 °C and that the Q2/Q3 ratio measured by Si NMR analysis of tobermorite decreased from 5.0 to 2.8, with a Al/(Al + Si) molar ratio of 0 to 0.10 in the starting mixture. However, in the quartz-lime system, the Q2/Q3 ratio was about 2.0, which corresponds to the ideal tobermorite structure [17]. Therefore, it is likely that Al accelerates formation of Q3 sites of the silicate chains under hydrothermal conditions. With Al addition, the prominent crystallization in the (002) direction of tobermorite, which was observed only in the case of the reactive silica system (the A series), is possibly attributable to the Al position in the silicate chains. However, Sakiyama et al. [17] have reported that the Q2/Q3 ratio of tobermorite increased with the Al/(Al + Si) ratio of the starting mixture in the quartz-lime system. According to our present model, reaction (I) in their experiments may reach completion because of the lower reactivity of the silica source; thus, Al might only affect the structure after tobermorite formation.

We should consider whether the nanostructure of C-S-H has an effect on tobermorite formation as well. Al acted as a linker for the silicate chains, thereby producing aluminosilicate chains with longer length in cement hydration [81]. However, Renaudin et al. reported that insertion of Al atoms in the C-S-H structure involved a disruption into the layered framework [82,83]. In the present study, it was not fully clarified how these phenomena influenced tobermorite formation. Thus, additional studies to reveal the role of Al in the C-S-H structure just before tobermorite formation are desirable.

In the present report, the increases and decreases of C-S-H and KA phases were mainly discussed; however, it should be noted that the formation of HE has an effect on reaction (II). For the experiment on A-5, HE remained until about the time of 400 min and unique behavior of anhydrite formation was observed during the same time period. As impurities in the liquid phase, SO_4^{2-} ions affected tobermorite formation under the hydrothermal conditions [19,31–34]. Thus, the clarification of the mechanism may be an important issue in the future.

4. Conclusions

Using an originally developed autoclave cell for *in situ* transmission XRD in combination with a high-energy synchrotron radiation source, the mechanism of tobermorite formation in the processing of AAC was successfully investigated. The effects of the reactivity of quartz in the raw material, as well as the effects of the addition of Al compound on tobermorite formation were studied.

In the experiments using reactive quartz as the silica source, tobermorite crystallized rapidly in the early stage of the autoclave process, but the formation reaction rate was decreased in the late stage, and C-S-H and KA phase remained at the end of the reaction period. On the other hand, in the experiments using less-reactive quartz, tobermorite continued to crystallize until the end and the final quantity of tobermorite became much larger than that in the reactive quartz system. According to the past studies, this implied that two types of C-S-H were involved in the present study. One type was formed in the less-reactive quartz system and readily crystallized to form tobermorite; the other type was formed in the reactive quartz system and did not readily crystallized to form tobermorite.

Al addition had a significant effect on tobermorite formation, especially the accelerated growth along the *c*-axis, which was clearly observed in the experiments with reactive quartz. On the other hand, Al addition did not affect the dissolution rate of quartz. In the system with a certain amounts of Al ions, tobermorite formation via KA was an important route, in the addition of the C-S-H route. KA decreased with the formation of tobermorite and simultaneously with the decrease of its own lattice constant. Therefore, KA was considered to play an important role in the liquid–solid reaction. It was suggested that Al addition affected the stability of the C-S-H and tobermorite structures.

A model for the mechanism of tobermorite formation was suggested; namely, the tobermorite formation route involves two pathways, via C-S-H and KA, and the reactions along each pathway influenced each other. Especially, the structure of the initially formed C-S-H affected the subsequent reactions. For example, the ions in the liquid phase affected KA formation and degradation, and affected tobermorite formation from the C-S-H phase.

Acknowledgment

This study was performed with the approval of the Japan Synchrotron Radiation Research Institute (Proposal Nos. 2008B1864 and 2009B1788).

References

[1] M.W. Grutzeck, Cellular concrete, in: M. Scheffler, P. Colombo (Eds.), Cellular Ceramics, Wiley-VCH, Weinheim, 2005, pp. 193–223.

[2] M. Haas, The future of AAC—from a material scientist's point of view, in: M.C. Limbachiya, J.J. Roberts (Eds.), Autoclaved Aerated Concrete, Taylor & Francis, London, 2005, pp. 187–193.

[3] G. Schober, Chemical transformations during the manufacturing of autoclaved aerated concrete (AAC): cement, lime, gypsum and quartz sand become cellular concrete, ZKG Int. 58 (2005) 63–70.

[4] J. Alexanderson, Relations between structure and mechanical properties of autoclaved aerated concrete, Cem. Concr. Res. 9 (1979) 507–514.

[5] T. Mitsuda, K. Sasaki, H. Ishida, Phase evolution during autoclaving process of aerated concrete, J. Am. Ceram. Soc. 75 (1992) 1858–1863.

[6] N. Isu, H. Ishida, T. Mitsuda, Influence of quartz particle size on the chemical and mechanical properties of autoclaved aerated concrete (I) tobermorite formation, Cem. Concr. Res. 25 (1995) 243–248.

[7] N.Y. Mostafa, Influence of air-cooled slag on physicochemical properties of autoclaved aerated concrete, Cem. Concr. Res. 35 (2005) 1349–1357.

[8] H. Sato, M. Grutzeck, Effect of starting materials on the synthesis of tobermorite, Mater. Res. Soc. Symp. Proc. 245 (1992) 235–240.

[9] T. Mitsuda, Influence of starting materials on the hydrothermal reaction in the $CaO–SiO_2–H_2O$ system (in Japanese), Ganseki Kobutsu Kosho Gakkaishi 3 (1982) 317–329.

[10] Y. Okada, N. Isu, T. Masuda, H. Ishida, Influence of starting materials on the formation of 1.1 nm tobermorite (in Japanese), J. Ceram. Soc. Jpn. 102 (1994) 1148–1153.

[11] S.A.S. El-Hemaly, T. Mitsuda, H.F.W. Taylor, Synthesis of normal and anomalous tobermorites, Cem. Concr. Res. 7 (1977) 429–438.

[12] G.L. Kalousek, Tobermorite and related phases in the system $CaO–SiO_2–H_2O$, J. Am. Concr. Inst. 26 (1955) 989–1011.

[13] G.L. Kalousek, A.F. Plebes, Crystal chemistry of hydrous calcium silicates: III, Morphology and other properties of tobermorite and related phases, J. Am. Ceram. Soc. 41 (1958) 124–132.

[14] C.F. Chan, M. Sakiyama, T. Mitsuda, Kinetics of the CaO–quartz–H_2O reaction at 120 to 180 °C in suspensions, Cem. Concr. Res. 8 (1978) 1–5.

[15] C.F. Chan, T. Mitsuda, Formation of 11 Å tobermorite from mixtures of lime and colloidal silica with quartz, Cem. Concr. Res. 8 (1978) 135–138.

[16] T. Mitsuda, H.F.W. Taylor, Influence of aluminium on the conversion of calcium silicate hydrate gels into 11 Å tobermorite at 90 °C and 120 °C, Cem. Concr. Res. 5 (1975) 203–210.

[17] M. Sakiyama, T. Maeshima, T. Mitsuda, Synthesis and crystal chemistry of Al-substituted 11 Å tobermorite, J. Soc. Inorg. Mater. Jpn. 7 (2000) 413–419.

[18] M. Sakiyama, T. Mitsuda, Hydrothermal reaction between C-S-H and kaolinite for the formation of tobermorite at 180 °C, Cem. Concr. Res. 7 (1977) 681–686.

[19] E.I. Al-Wakeel, S.A. El-Korashy, Reaction mechanism of the hydrothermally treated $CaO–SiO_2–Al_2O_3$ and $CaO–SiO_2–Al_2O_3–CaSO_4$ systems, J. Mater. Sci. 31 (1996) 1909–1913.

[20] T. Mitsuda, H. Toraya, Y. Okada, M. Shimoda, Synthesis of tobermorite: NMR spectroscopy and analytical electron microscopy, Ceram. Trans. 5 (1989) 206–213;
Y. Okada, M. Shimoda, T. Mitsuda, H. Toraya, Synthesis of tobermorite: NMR spectroscopy and analytical electron microscopy, J. Res. Onoda Cement Co. 42 (2) (1990) 199–206.

[21] S. Komarneni, D.M. Roy, R. Roy, Al-substituted tobermorite: shows cation exchange, Cem. Concr. Res. 12 (1982) 773–780.

[22] G.L. Kalousek, Crystal chemistry of hydrous calcium silicates: I, Substitution of aluminum in lattice of tobermorite, J. Am. Ceram. Soc. 40 (1957) 74–80.

[23] S. Komarneni, R. Roy, D.M. Roy, C.A. Fyfe, C.J. Kennedy, A.A. Bother-By, J. Dadok, A. S. Chesnick, ^{27}Al and ^{29}Si magic angle spinning nuclear magnetic resonance spectroscopy of Al-substituted tobermorites, J. Mater. Sci. 20 (1985) 4209–4214.

[24] S. Komarneni, M. Tsuji, Selective cation exchange in substituted tobermorites, J. Am. Ceram. Soc. 72 (1989) 1668–1674.

[25] M. Tsuji, S. Komarneni, P. Malla, Substituted tobermorites: ^{27}Al and ^{29}Si MAS NMR, cation exchange, and water sorption studies, J. Am. Ceram. Soc. 74 (1991) 274–279.

[26] H. Youssef, D. Ibrahim, S. Komarneni, K.J.D. Mackenzie, Synthesis of 11 Å Al-substituted tobermorite from trachyte rock by hydrothermal treatment, Ceram. Int. 36 (2010) 203–209.

[27] L. Black, A. Stumm, K. Garbev, P. Stemmermann, K.R. Hallam, G.C. Allen, X-ray photoelectron spectroscopy of aluminium-substituted tobermorite, Cem. Concr. Res. 35 (2005) 51–55.

[28] R. Gabrovšek, B. Kurbus, D. Mueller, W. Wieker, Tobermorite formation in the system CaO, $C_3S–SiO_2–Al_2O_3–NaOH–H_2O$ under hydrothermal conditions, Cem. Concr. Res. 23 (1993) 321–328.

[29] M.W. Barnes, B.E. Scheetz, The chemistry of Al-tobermorite and its coexisting phases at 175 °C, Mater. Res. Soc. Symp. Proc. 179 (1991) 243–272.

[30] J. Reinik, I. Heinmaa, J. Mikkola, U. Kirso, Hydrothermal alkaline treatment of oil shale ash for synthesis of tobermorite, Fuel 86 (2007) 669–676.

[31] N.Y. Mostafa, A.A. Shaltout, H. Omar, S.A. Abo-El-Enein, Hydrothermal synthesis and characterization of aluminium and sulphate substituted 1.1 nm tobermorite, J. Alloy. Compd. 467 (2009) 332–337.

[32] M. Sakiyama, Y. Oshio, T. Mitsuda, Influence of gypsum on the hydrothermal reaction of lime–quartz system and on the strength of autoclaved calcium silicate product, J. Soc. Inorg. Mater. Jpn. 7 (2000) 685–691.

[33] Z. Sauman, F. Vavrin, Condition of the hydroxyl ellestadite formation in mixtures containing calcium sulphate, Proceedings 7th International Congress on the Chemistry of Cement, Paris, 1980, pp. II 106–II 110.

[34] K. Baltakys, Influence of gypsum additive on the formation of calcium silicate hydrates in mixtures with $C/S = 0.83$ or 1.0, Mater. Sci. Poland 27 (2009) 1091–1101.

[35] R. Kondo, Kinetic study on hydrothermal reaction between lime and silica, in: International Symposium Autoclaved Calcium Silicate Building Products, London, 1965, 1967, pp. 92–97.

[36] K. Asaga, K.H. Lee, T. Kamei, M. Daimon, Hydrothermal reaction in $CaO–SiO_2$, Proceeding of the International Hydrothermal Reaction, 1st, Yokohama, Japan, 1982, pp. 839–848.

[37] V. Alujevic, A. Bezjak, A. Glasnovic, Kinetic study of the hydrothermal reaction in CaO–quartz system, Cem. Concr. Res. 16 (1986) 695–699.

[38] J.H. Houston, R.S. Maxwell, S.A. Carroll, Transformation of meta-stable calcium silicate hydrates to tobermorite: reaction kinetics and molecular structure from XRD and NMR spectroscopy, Geochem. Trans. 10 (2009) 1.

[39] M. Huber, K.T. Fehr, S.G. Zuern, Kinetics of Al-tobermorite formation under hydrothermal conditions, Proceedings of Joint 6th International Symposium on Hydrothermal Reactions and 4th International Conference on Solvo-Thermal Reactions, Kochi, Japan, 2000, pp. 274–277.

[40] K.T. Fehr, S.G. Zuern, Mechanisms of calcium-silicate-hydrates formation under hydrothermal conditions, Proceedings of Joint 6th International Symposium on Hydrothermal Reactions and 4th International Conference on Solvo-Thermal Reactions, Kochi, Japan, 2000, pp. 278–281.

[41] K.T. Fehr, M. Huber, S.G. Zuern, E. Peters, Determination of the reaction kinetics and mechanism of Al-tobermorite under hydrothermal condition by in-situ neutron diffraction, Proceedings of 7th International Symposium on Hydrothermal Reactions, Changchun, China, 2003, pp. 19–25.

[42] S. Shaw, S.M. Clark, C.M.B. Henderson, Hydrothermal formation of the calcium silicate hydrates, tobermorite ($Ca_5Si_6O_{16}(OH)_2$-$4H_2O$) and xonotlite ($Ca_6Si_6O_{17}(OH)_2$): an in-situ synchrotron study, Chem. Geol. 167 (2000) 129–140.

[43] P. Norby, A.N. Christensen, J.C. Hanson, In-situ studies of zeolite synthesis using powder diffraction methods. Crystallization of “instant zeolite A” powder and synthesis of CoAPO-5, Stud. Surf. Sci. Catal. 84 (1994) 179–186.

[44] A.N. Christensen, T.R. Jensen, J.C. Hanson, Formation of ettringite, $Ca_6Al_2(SO_4)_3(OH)_{12}$-$26H_2O$, AFt, and monosulfate, $Ca_4Al_2O_6(SO_4)$-$14H_2O$, AFm-14, in hydrothermal hydration of Portland cement and of calcium aluminum oxide—calcium sulfate dihydrate mixtures studied by in-situ synchrotron X-ray powder diffraction, J. Solid State Chem. 177 (2004) 1944–1951.

[45] T.R. Jensen, A.N. Christensen, J.C. Hanson, Hydrothermal transformation of the calcium aluminum oxide hydrates $CaAlO_4$-$10H_2O$ and $Ca_2Al_2O_5$-$8H_2O$ to $Ca_3Al_2(OH)_{12}$ investigated by in situ synchrotron X-ray powder diffraction, Cem. Concr. Res. 35 (2005) 2300–2309.

[46] A.C. Jupe, A.P. Wilkinson, K. Luke, G.P. Funkhouser, Class H oil well cement hydration at elevated temperatures in the presence of retarding agents: an in situ high-energy X-ray diffraction study, Ind. Eng. Chem. Res. 44 (2005) 5579–5584.

[47] A.C. Jupe, A.P. Wilkinson, K. Luke, G.P. Funkhouser, Class H cement hydration at 180 °C and high pressure in the presence of added silica, Cem. Concr. Res. 38 (2008) 660–666.

[48] R. Snellings, G. Mertens, S. Hertsens, J. Elsen, The zeolite-lime pozzolanic reaction kinetics and products by in situ synchrotron X-ray powder diffraction, Microporous Mesoporous Mater. 126 (2009) 40–49.

[49] P. Norby, In-situ XRD as a tool to understanding zeolite crystallization, Curr. Opin. Colloid Interface Sci. 11 (2006) 118–125.

[50] D. O'Hare, J.S.O. Evans, R.J. Francis, P.S. Halasyamani, P. Norby, J. Hanson, Time-resolved, in-situ X-ray diffraction studies of the hydrothermal synthesis of microporous materials, Microporous Mesoporous Mater. 21 (1998) 253–262.

[51] P. Barnes, S.L. Colston, A.C. Jupe, S.D.M. Jacques, M. Attfield, R. Pisulla, S. Morgan, C. Hall, P. Livesey, S. Lunt, The use of synchrotron sources in the study of cement materials, in: J. Bensted, P. Barnes (Eds.), Structure and Performance of Cements, 2nd Ed, Spon Press, London, 2002, pp. 477–499.

[52] N. Meller, C. Hall, K. Kyritsis, G. Giriat, Synthesis of cement based $CaO–Al_2O_3–SiO_2–H_2O$ (CASH) hydroceramics at 200 and 250 °C: ex-situ and in-situ diffraction, Cem. Concr. Res. 37 (2007) 823–833.

[53] J. Kikuma, M. Tsunashima, T. Ishikawa, S. Matsuno, A. Ogawa, K. Matsui, M. Sato, Hydrothermal formation of tobermorite studied by in situ X-ray diffraction under autoclave condition, J. Synchrotron Radiat. 16 (2009) 683–686.

[54] J. Kikuma, M. Tsunashima, T. Ishikawa, S. Matsuno, A. Ogawa, K. Matsui, M. Sato, In-situ time-resolved X-ray diffraction of tobermorite formation process under autoclave condition, J. Am. Ceram. Soc. 93 (2010) 2667–2674.

[55] I. Hattori, M. Umeda, Crystallinity indices of quartz in chert of Central Japan: their reliability and some geological applications, Bull. Fukui City Mus. Nat. His. 55 (2008) 17–32.

[56] K.J. Murata, M.B. Norman II, An index of crystallinity for quartz, Am. J. Sci. 276 (1976) 1120–1130.

[57] Y. Wakizaka, Alkali–silica reactivity of Japanese rocks, Eng. Geol. 56 (2000) 211–221.

[58] ASTM, ASTM C150/C 150M-09, Standard Specification for Portland Cement, ASTM, West Conshohocken, PA, 2009.

[59] H.F.W. Taylor, Hydration of the calcium silicate phases, Cement Chemistry, 2nd edition, Thomas Telford, London, 1997, pp. 113–156.

[60] P.M. Dove, Kinetic and thermodynamic controls on silica reactivity in weathering environments, in: A.F. White, S.L. Brantley (Eds.), Reviews in Mineralogy, vol. 31, Mineralogical Society of America, Washington, DC, 1995, pp. 235–290.

[61] B.R. Bickmore, K.L. Nagy, A.K. Gray, A.R. Brinkerhoff, The effect of $Al(OH)_4^-$ on the dissolution rate of quartz, Geochim. Cosmochim. Acta 70 (2006) 290–305.

[62] X. Cong, R.J. Kirkpatrick, ^{29}Si MAS NMR study of the structure of calcium silicate hydrate, Adv. Cem. Based Mater. 3 (1996) 144–156.

[63] J.J. Chen, J.J. Thomas, H.F.W. Taylor, H.M. Jennings, Solubility and structure of calcium silicate hydrate, Cem. Concr. Res. 34 (2004) 1499–1519.

[64] I.G. Richardson, Tobermorite/jennite- and tobermorite/calcium hydroxide-based models for the structure of C-S-H: applicability to hardened pastes of tricalcium silicate, β-dicalcium silicate, Portland cement, and blends of Portland cement with blast-furnace slag, metakaolin or silica fume, Cem. Concr. Res. 34 (2004) 1733–1777.

[65] A. Nonat, The structure and stoichiometry of C-S-H, Cem. Concr. Res. 34 (2004) 1521–1528.

[66] Y. Okada, H. Ishida, T. Mitsuda, ^{29}Si NMR spectroscopy of silicate anions in hydrothermally formed C-S-H, J. Am. Ceram. Soc. 77 (1994) 765–768.

[67] F. Pertlik, Bibliography of hibschite, a hydrogarnet of grossular type, GeoLine 15 (2003) 113–119.

[68] D.S. Klimesch, A. Ray, Effects of quartz particle size on hydrogarnet formation during autoclaving at 180 °C in the $CaO–Al_2O_3–SiO_2–H_2O$ system, Cem. Concr. Res. 28 (1998) 1309–1316.

[69] D.S. Klimesch, A. Ray, Effects of quartz particle size and kaolin on hydrogarnet formation during autoclaving, Cem. Concr. Res. 28 (1998) 1317–1323.

[70] C.A. Rios, C.D. Williams, M.A. Fullen, Hydrothermally synthesis of hydrogarnet and tobermorite in the $CaO–Al_2O_3–SiO_2–H_2O$ system: a comparative study, Appl. Clay Sci. 43 (2009) 228–237.

[71] D.G. Bennett, D. Read, M. Atkins, F.P. Glasser, A thermodynamic model for blended cements. II: cement hydrate phases; thermodynamic values and modelling studies, J. Nucl. Mater. 190 (1992) 315–325.

[72] R. Siauciunas, A. Baltusnikas, Influence of SiO_2 modification on hydrogarnets formation during hydrothermal synthesis, Cem. Concr. Res. 33 (2003) 1789–1793.

[73] J.M. Rivas-Mercury, P. Pena, A.H. de Aza, X. Tortillas, Dehydration of $Ca_3Al_2(SiO_4)_y(OH)_{4(3-y)}$ ($0<y<0.176$) studied by neutron thermodiffractometry, J. Euro. Ceram. Soc. 28 (2008) 1737–1748.

[74] S.Y. Hong, F.P. Glasser, Alkali binding in cement pastes: part I. The C-S-H phase, Cem. Concr. Res. 29 (1999) 1893–1903.

[75] S.Y. Hong, F.P. Glasser, Alkali sorption by C-S-H and C-A-S-H gels: part II. Role of alumina, Cem. Concr. Res. 32 (2002) 1101–1111.

[76] G.K. Sun, J.F. Young, R.J. Kirkpatrick, The role of Al in C-S-H: NMR, XRD, and compositional results for precipitated samples, Cem. Concr. Res. 36 (2006) 18–26.

[77] M. Grutzeck, A. Benesi, B. Fanning, Silicon-29 magic angle spinning nuclear magnetic resonance study of calcium silicate hydrates, J. Am. Ceram. Soc. 72 (1989) 665–668.

[78] P. Faucon, T. Charpentier, A. Nonat, J.C. Petit, Triple-quantum two-dimensional ^{27}Al magic angle nuclear magnetic resonance study of the aluminum incorporation in calcium silicate hydrates, J. Am. Chem. Soc. 120 (1998) 12075–12082.

[79] I.G. Richardson, G.W. Groves, The structure of the calcium silicate hydrate phases present in hardened pastes of white Portland cement/blast-furnace blends, J. Mater. Sci. 32 (1997) 4793–4802.

[80] K. Sasaki, T. Masuda, H. Ishida, T. Mitsuda, Structural degradation of tobermorite during vibratory milling, J. Am. Ceram. Soc. 79 (1996) 1569–1574.

[81] M.D. Andersen, H.J. Jacobson, J. Skibsted, Characterization of white Portland cement hydration and the C-S-H structure in the presence of sodium aluminate by ^{27}Al and ^{29}Si MAS NMR spectroscopy, Cem. Concr. Res. 34 (2004) 857–868.

[82] G. Renaudin, J. Russias, F. Leroux, F. Frizon, C. Cau-Dit-Coumes, Structural characterization of C-S-H and C-A-S-H samples—part I: long-range order investigated by Rietveld analyses, J. Solid State Chem. 182 (2009) 3312–3319.

[83] G. Renaudin, J. Russias, F. Leroux, C. Cau-Dit-Coumes, F. Frizon, Structural characterization of C-S-H and C-A-S-H samples—part II: local environment investigated by spectroscopic analyses, J. Solid State Chem. 182 (2009) 3320–3329.